Emergence of singular structures in Oldroyd-B fluids

Becca Thomases and Michael Shelley
Courant Institute of Mathematical Sciences, New York University, New York, New York 10012, USA

(Received 10 November 2006; accepted 7 August 2007; published online 11 October 2007)

Numerical simulations reveal the formation of singular structures in the polymer stress field of a viscoelastic fluid modeled by the Oldroyd-B equations driven by a simple body force. These singularities emerge exponentially in time at hyperbolic stagnation points in the flow and their algebraic structure depends critically on the Weissenberg number. Beyond a first critical Weissenberg number the stress field approaches a cusp singularity, and beyond a second critical Weissenberg number the stress becomes unbounded exponentially in time. A local approximation to the solution at the hyperbolic point is derived from a simple ansatz, and there is excellent agreement between the local solution and the simulations. Although the stress field becomes unbounded for a sufficiently large Weissenberg number, the resultant forces of stress grow subexponentially. Enforcing finite polymer chain lengths via a FENE-P penalization appears to keep the stress bounded, but a cusp singularity is still approached exponentially in time. © *2007 American Institute of Physics*. [DOI: 10.1063/1.2783426]

I. INTRODUCTION

Recent experimental work[1–4] on the mixing of viscoelastic fluids at low Reynolds number has led us to consider the Oldroyd-B model for viscoelastic fluids in the zero Reynolds number limit for a standard curvilinear flow. We will report on results for mixing in a future article, but while investigating this phenomenon we have observed the formation of singular structures in dynamical solutions of the Oldroyd-B equations, which we report on here. The Oldroyd-B equations are a popular continuum model of a so-called "Boger" fluid, having a simple and elegant structure but also some well documented flaws; see, for example, Refs. 5–8 and also Ref. 9. The Oldroyd-B equations can be derived from microscopic principles by assuming a linear Hooke's law for the restoring force under distension of immersed polymer coils; see Ref. 10. The Oldroyd-B model is often criticized for this simplification because the linear Hooke's law puts no restriction on the length of polymer chains. Related to this, in an extensional rheological flow the steady Oldroyd-B equations can exhibit stress divergences.[9] Here we consider low Reynolds number flow with biperiodic boundary conditions using the Stokes–Oldroyd-B equations. This allows us to use a spectral method to evolve the system that is helpful to deduce the analytic structure of the flow and monitor the numerical accuracy of solutions. The geometry of the flow is set up with a time-independent background force, which in the pure Newtonian case yields the four-roll mill. In the full nonlinear system, the polymer stress acts as an additional force that drives the evolution of the fluid velocity.

The four-roll mill geometry of the flow creates a central hyperbolic stagnation point. This type of flow geometry was first used by Taylor[11] and subsequently made popular by Leal and others.[12] The four-roll mill consists of four cylinders that rotate to create a stagnation point between the rollers, and with different rotation direction and speed one can create an arbitrary linear flow field at this central point.[13] We create a numerical idealization of this geometry for the case of a two-dimensional extensional flow. At the extensional points in the flow we find the emergence, exponentially in time, of singular structures in the stresses at every Weissenberg number. These singular structures appear as "stress islands" in the diagonal components of the stress tensor that lie along the unstable manifold (or outgoing streamline) associated with the stagnation point. The regularity of the singular structures decreases as the Weissenberg number increases. For sufficiently small Weissenberg number, these singularities appear only in high derivatives of the stress tensor. There are two significant transitions as the Weissenberg number is increased. The first is characterized by the onset of a near cusp in the stress field centered at the hyperbolic stagnation point. This becomes sharper in time, and our simulations suggest that a cusp is approached exponentially in time. As the Weissenberg number increases further, this cusp "breaks," resulting in unbounded solutions. Again, it appears that the unbounded solutions are approached exponentially in time. Furthermore, for a sufficiently large Weissenberg number the rate at which the solution becomes singular decreases in the Weissenberg number.

In these simulations, we find that the velocity rapidly approaches a steady state that remains locally, about the central hyperbolic point, a simple straining flow. This enables us to posit a local solution that agrees remarkably well with our computations. Solutions of this type have been observed previously for steady flows, and their structure is related directly to an imposed background flow; see Refs. 5 and 14. Here we study how these singular structures are selected and approached as well as their association with ancillary flow structures. We also observe that the singularities appear to remain integrable in accordance with the finiteness of the system's strain energy. We present a similar analysis of the FENE-P penalization.

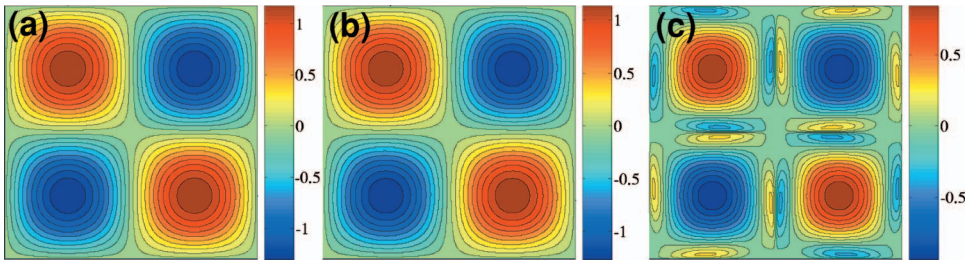

FIG. 1. (Color) Contour plots of vorticity in a periodic cell at $t=6$: (a) $\mathcal{W}i=0.3$, (b) $\mathcal{W}i=0.6$, (c) $\mathcal{W}i=5.0$.

II. EQUATIONS OF MOTION

We study numerically the two-dimensional Oldroyd-B equations of viscoelastic flow in the low Reynolds number limit. Biperiodic boundary conditions are assumed and persistent curvilinear flows are created by imposing a very simple body force. The Stokes–Oldroyd-B equations are given by

$$-\nabla p+\Delta\mathbf{u}=-\beta\nabla\cdot\mathbf{S}+\mathbf{f}\quad\text{and}\quad\nabla\cdot\mathbf{u}=0, \tag{1}$$

$$\partial_t\mathbf{S}+\mathbf{u}\cdot\nabla\mathbf{S}-(\nabla\mathbf{u}\,\mathbf{S}+\mathbf{S}\nabla\mathbf{u}^T)+\frac{1}{\mathcal{W}i}(\mathbf{S}-\mathbf{I})=0, \tag{2}$$

where $\mathrm{Wi}=\tau_p/\tau_f$ is the Weissenberg number, with τ_p the polymer relaxation time and τ_f the time scale of the fluid flow. The dimensional scaling F of the forcing $\mathbf{f}$ is used to set the flow time scale as $\tau_f=\mu/\rho LF$, where μ is the solvent viscosity, ρ is the fluid density, and L is the system size. This sets the adimensional force, and the time scale of transport, to be order 1. The parameter $\beta=G\tau_f/\mu$ measures the relative contribution of the polymer stress to momentum balance, where G is the isotropic stress in the polymer field in the absence of flow. Note that Eq. (2) preserves symmetry and positivity of $\mathbf{S}$, as is expected given its microscopic derivation.[9] The force used here is given by

$$\mathbf{f}=\begin{pmatrix}2\sin x\cos y\\-2\cos x\sin y\end{pmatrix}. \tag{3}$$

In a purely Newtonian Stokes flow ($\beta=0$), this forcing yields a four-vortex "mixer" in each $[0,2\pi]^2$ cell, like that shown in Fig. 1(a), with the velocity given by

$$\mathbf{u}=\begin{pmatrix}-\sin x\cos y\\\cos x\sin y\end{pmatrix}. \tag{4}$$

In our simulations, we fix the ratio of polymer viscosity to solvent viscosity (which corresponds to $\beta\cdot\mathcal{W}i$). For the majority of our simulations, we will consider the case $\beta\cdot\mathcal{W}i=1/2$, however we will make some comments regarding other values in Sec. V. The value $\beta\cdot\mathcal{W}i=1/2$ is consistent with the fluids used in recent experiments of dilute polymer solutions with highly viscous solvents, "Boger fluids" (see, for example, Ref. 4). The solution viscosity is 1.2 Pa s, while the solvent (97% glycerol/water) is 0.8 Pa s, yielding $\beta\cdot\mathcal{W}i=(1.2-0.8)/0.8=0.5$).

The stress tensor $\mathbf{S}$ is a symmetric 2-tensor, with elements S_{ij}, $i\leqslant j=1,2$, whose trace, tr$\mathbf{S}$, is an important physical quantity representing the amount of stretching of polymer coils. With the force given in Eq. (3), and initial data $\mathbf{S}(0)=\mathbf{I}$, many symmetries and relations are maintained in the evolving solution, such as $S_{22}(x,y)=S_{11}(y+\pi,x+\pi)$. These symmetries together with the background force $\mathbf{f}$ create a persistent hyperbolic stagnation point in the velocity field. We will refer to the stagnation point at (π,π), at which there is extension in the x direction and compression in the y direction, as the *central hyperbolic point*.

The system (1) and (2) has an energy, the "strain energy," given by

$$\mathcal{E}\equiv\frac{1}{2}\int\int\mathrm{tr}(\mathbf{S}-\mathbf{I})dxdy,$$

which satisfies

$$\dot{\mathcal{E}}+\frac{1}{\mathcal{W}i}\mathcal{E}=-\frac{1}{\beta}\int\int|\nabla\mathbf{u}|^2dxdy-\frac{1}{\beta}\int\int\mathbf{u}\cdot\mathbf{f}dxdy. \tag{5}$$

The second term on the right-hand side is the power input to the system by the forcing. If it remains bounded, say by C, then $\dot{\mathcal{E}}+(1/\mathcal{W}i)\mathcal{E}\leqslant C/\beta$, which upon integration yields the bound

$$\mathcal{E}(t)\leqslant\frac{C\,\mathcal{W}i}{\beta}+C_1e^{-t/\mathcal{W}i}. \tag{6}$$

Perhaps surprisingly, Eqs. (1) and (2) are not controlled by a diffusion. To see this, consider a linearized version of Eqs. (1) and (2), where

$$\mathbf{f}=\epsilon\mathbf{g},\quad\mathbf{u}=\epsilon\mathbf{v},\quad p=\epsilon\mathbf{r},\quad\text{and}\ \mathbf{S}=\mathbf{I}+\epsilon\mathbf{T}$$

for $\epsilon\ll1$. The linearized equations are

$$\begin{aligned}&-\nabla\mathbf{r}+\Delta\mathbf{v}=-\beta\nabla\cdot\mathbf{T}+\mathbf{g},\quad\nabla\cdot\mathbf{v}=0,\\&\partial_t\mathbf{T}-(\nabla\mathbf{v}+\nabla\mathbf{v}^T)+\frac{1}{\mathcal{W}i}\mathbf{T}=0.\end{aligned} \tag{7}$$

Using the Fourier transform to solve the linearized equations, the evolution of $\hat{\mathbf{T}}$ is given by

$$\partial_t\hat{\mathbf{T}}+\mathbf{L}\left(\frac{k}{|k|}\right)\hat{\mathbf{T}}+\mathbf{P}(k)\hat{\mathbf{g}}=0, \tag{8}$$

where $\mathbf{L}$ is a linear tensorial operator on the normalized wave vector. Thus, there is no scale-dependent dissipation in the evolution equation for $\mathbf{T}$. This lack of scale-dependent dissipation is one source of difficulty in existence results for these equations (and for numerical difficulties as well). In two and three dimensions, the system is known to have global solutions for small (perturbative) initial data, where the size of the solution depends on the viscosity; however, there

are no results for global existence if the initial data are large, even for two dimensions; see Refs. 15–18.

With the constraint $\beta \cdot \mathcal{W}i = C$, one can examine the formal limits, $\mathcal{W}i \to 0$ and $\mathcal{W}i \to \infty$. For $\mathcal{W}i \ll 1$, let

$$\mathbf{u} = \mathcal{W}i\mathbf{v} + \text{h.o.t.}, \quad \text{and } \mathbf{S} = \mathbf{I} + \mathcal{W}i\mathbf{T} + \text{h.o.t.}$$

Solving for the leading term in the evolution of $\mathbf{S}$ in Eq. (2) gives

$$\mathbf{T} = \mathcal{W}i(\nabla\mathbf{v} + \nabla\mathbf{v}^T) \Rrightarrow \beta\nabla \cdot \mathbf{T} = C\Delta\mathbf{v}.$$

Hence, in the limit, $\mathbf{v}$ solves the Stokes equation with viscosity $(1+C)$.

Next consider $\mathcal{W}i \gg 1$ and $t \sim \mathcal{O}(1)$. In this formal limit (namely $\mathcal{W}i \to \infty$ with $t \ll \mathcal{W}i$), the equations decouple, the velocity $\mathbf{v}$ satisfies the Stokes equation with viscosity 1, and the stress satisfies $\mathbf{T} = \mathbf{F}\mathbf{T}(0)\mathbf{F}^T$, where $\mathbf{F}$ is the deformation gradient and satisfies the equation

$$\partial_t\mathbf{F} + \mathbf{v} \cdot \nabla\mathbf{F} = \nabla\mathbf{v}\mathbf{F}.$$

Since $\mathbf{v}$ is steady, this is a linear equation for the deformation gradient. Although both limits $\mathcal{W}i \to 0$ and $\mathcal{W}i \to \infty$ give the Stokes flow for the velocity, there is very interesting (non-Stokesian) behavior for fixed finite $\mathcal{W}i$, and certainly as $\mathcal{W}i \to \infty$, for $t \gtrsim \mathcal{O}(\mathcal{W}i)$.

We solve the system (1) and (2) with a pseudospectral method. The stress $\mathbf{S}$ is evolved using a second-order Adams-Bashforth method. Given $\mathbf{S}$, the Stokes equation is easily inverted in Fourier space for $\mathbf{u}$. Given $\mathbf{u}$, the nonlinearities of the stress evolution, Eq. (2), are evaluated using a smooth filter that is applied in Fourier space before the quadratic terms are multiplied in real space; see Ref. 19 for details. The standard pseudospectral method was marginally unstable, but the introduction of the filter added stability. The smooth filter we use gives marginally more accurate results over a more standard 2/3 rule de-aliasing (see Ref. 20), and it yields smoother spectra for analysis. Care must be taken to maintain good spatial and temporal resolution as the evolving stress field becomes more singular. The spatial discretization is typically doubled as the active part of its spectrum approaches the onset of the filter in phase space. Maximal resolutions are 4096^2, and the simulations are stopped before the high wave-number part of the spectrum exceeds 10^{-5}. We find the positive definiteness is maintained in all of our simulations and the time-stepping was verified to have second-order accuracy.

III. LOCAL SOLUTION

Before we turn fully to the results of the numerical simulations, we discuss a solution to the system in Eqs. (1) and (2) that can be derived from a very simple ansatz. Assuming that the fluid velocity is the steady extensional flow

$$\mathbf{u} = \alpha(x, -y), \tag{9}$$

then the partial differential equation for the stress $\mathbf{S}$ decouples and each component of the stress field can be solved for independently. We first discuss the solution for S_{11}, which in the context of the local solution we refer to as γ. Then from Eq. (2), γ must satisfy the linear variable coefficient partial differential equation,

$$\partial_t\gamma + \alpha x\gamma_x - \alpha y\gamma_y + \left(\frac{1}{\mathcal{W}i} - 2\alpha\right)\gamma - \frac{1}{\mathcal{W}i} = 0.$$

Scaling time as $\mathcal{W}i \cdot t$ and setting $\epsilon = \alpha \cdot \mathcal{W}i$ gives

$$\partial_t\gamma + \epsilon x\gamma_x - \epsilon y\gamma_y + (1-2\epsilon)\gamma - 1 = 0. \tag{10}$$

This partial differential equation is solved by the method of characteristics with its general solution given by

$$\gamma(x,y,t) = \frac{1}{(1-2\epsilon)} + e^{(2\epsilon-1)t}H_{11}(xe^{-\epsilon t}, ye^{\epsilon t}) \tag{11}$$

for an arbitrary function H_{11}. We are interested in solutions that yield a time-independent algebraically singular structure on a collapsing length scale in y as $t \to \infty$, and which show little dependence on x. Hence we consider $H_{11}(a,b) \equiv h(b)$, where $h(b) \sim |b|^q$ as $b \to \infty$ for an arbitrary exponent q. One example would be

$$h(b) = h_0(1 + Cy^2e^{2\epsilon t})^{q/2}.$$

We determine the exponent q by requiring loss of time dependence of γ for large times, yielding $q = (1-2\epsilon)/\epsilon$, and large-time local solution

$$\gamma_\infty = \frac{1}{1-2\epsilon} + A|y|^{(1-2\epsilon)/\epsilon}. \tag{12}$$

Note that for $q < 0$ $(\epsilon > 1/2)$, these solutions have infinite stress at the origin, and that for $0 < q < 1$ $(1/3 < \epsilon < 1/2)$, these solutions are not differentiable at the origin. Solutions of the form in Eq. (12) are not new. Rallison and Hinch[5] observed that the stress field would support such singularities in a steady extensional flow; see also Renardy.[14] Both of those works consider the steady problem with an unconstrained strain rate α, which is somewhat different from the case we consider as we will ultimately let the system evolution select α.

The ansatz in Eq. (9) is not a solution to the Oldroyd-B equations in the periodic case, as it is only a valid approximation locally for a steady velocity. Although our numerical simulations are dynamic, we do observe that *locally*, near the hyperbolic stagnation points in the flow, the velocity rapidly approaches a steady state of the form given by Eq. (9), where the local strain rate α depends on the Weissenberg number. Figures 1(a)–1(c) show contour plots of the vorticity in a periodic cell for three different Weissenberg numbers at a fixed time $t=6$. Figures 2(a)–2(c) show contour plots of tr$\mathbf{S}$ at the same time, and we see that as the Weissenberg number is increased, the stress concentrates on thinner sets along the outgoing stagnation streamline. Slices of the velocity for $\mathcal{W}i = 5.0$ along the stable and unstable manifold of the central hyperbolic point are shown in Figs. 3(a) and 3(b). (For $\mathcal{W}i < 5.0$, the behavior is similar.) These show the effect of the elastic stresses on the flow. The velocity on the outgoing and incoming streamlines maintains the essentially sinusoidal structure while the magnitude drops by more than a factor of 5. Plots of the local strain rate α as a function of time for various Weissenberg number are given in Fig. 3(c). We ob-

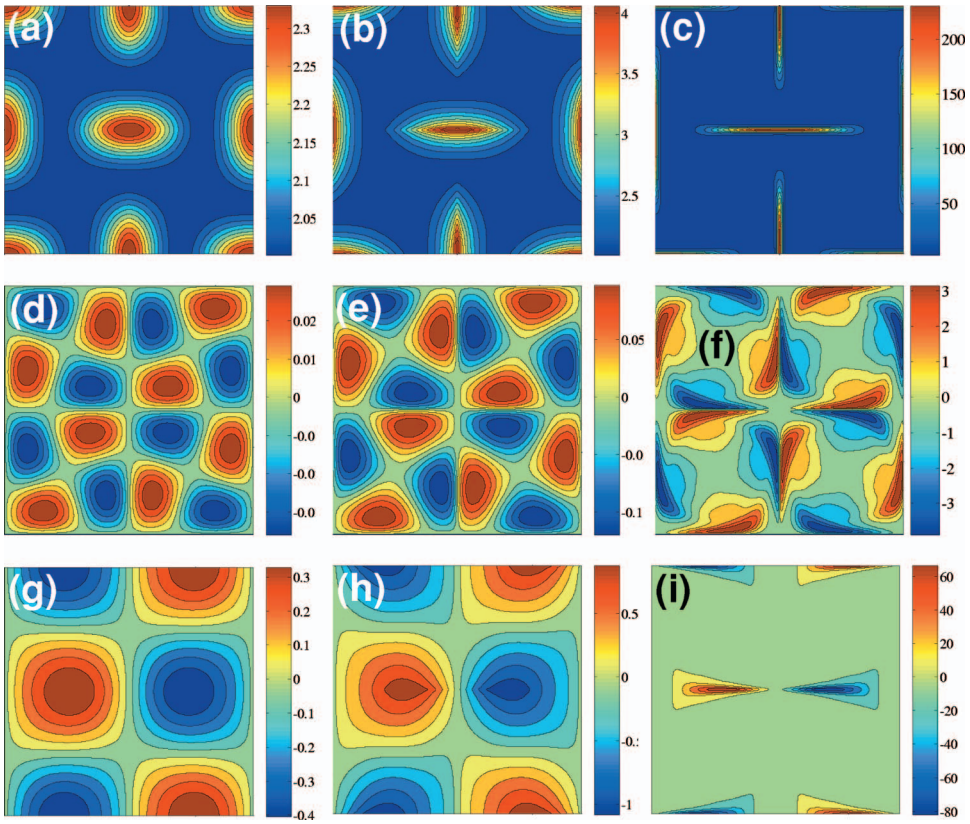

FIG. 2. (Color) (a)–(c) Contour plots of tr**S** for $\mathcal{W}i=0.3$, 0.6, and 5.0, from left to right, at $t=6$. S_{11} dominates at the central hyperbolic point, and S_{22} dominates at the hyperbolic point at $(0,\pi)$. (d)–(f) Contour plots of S_{12} for the same values of $\mathcal{W}i$ and time. (g)–(i) Contour plots of the first component of the force due to the polymer stress, $\nabla\cdot(\mathbf{S})_1=\partial_x S_{11}+\partial_y S_{12}$ for the same values of $\mathcal{W}i$ and time. Note the difference in scale in each case as $\mathcal{W}i$ is increased.

serve that α decreases in time to an apparently steady value. Taking this steady value as our parameter α, we see that α decreases in Weissenberg number [Fig. 4(a)]. We observe that as $\mathcal{W}i\to 0$, $\alpha\to 2/3$. This is in agreement with the formal limit $\mathcal{W}i\to 0$ discussion from Sec. II, where $\mathbf{u}$ solves the Stokes equation with viscosity $(1+C)$, and $C=1/2$.

The solution γ involves a rescaled time, and an "effective" Weissenberg number ϵ ("effective" because it scales the actual Weissenberg number by the local rate of strain at the hyperbolic point). Critical values of the exponent q occur when $(1-2\epsilon)/\epsilon=1\Rightarrow\epsilon_1=1/3$ and $(1-2\epsilon)/\epsilon=0\Rightarrow\epsilon_2=1/2$. The first critical value indicates that the solution is approaching a cusp singularity and corresponds to $\mathcal{W}i\approx 0.5$, the second critical value indicates that the solution is approaching a divergent singularity and corresponds to $\mathcal{W}i\approx 0.9$. If the solution is to remain integrable, it must be that $\epsilon<1$. Figure 4(b) shows the computed value of $\epsilon=\alpha\mathcal{W}i$, with the value of α coming from our simulations. It appears that $\epsilon<1$, which implies that the theoretical exponent $q=(1-2\epsilon)/\epsilon>-1$, and hence the solutions are integrable. The elastic stresses appear to be modifying the flow to maintain this integrability as is required by the energy bound [recall Eq. (6)]. This observation was also made in Ref. 21. The "effective" Weissenberg number, ϵ, also gives information about the exponential rates of both decay and divergence, the maximum values of the stresses (when bounded), and the inner scaling of the stress field.

The approximation $\mathbf{u}=\alpha(x,-y)$ yields local solutions for

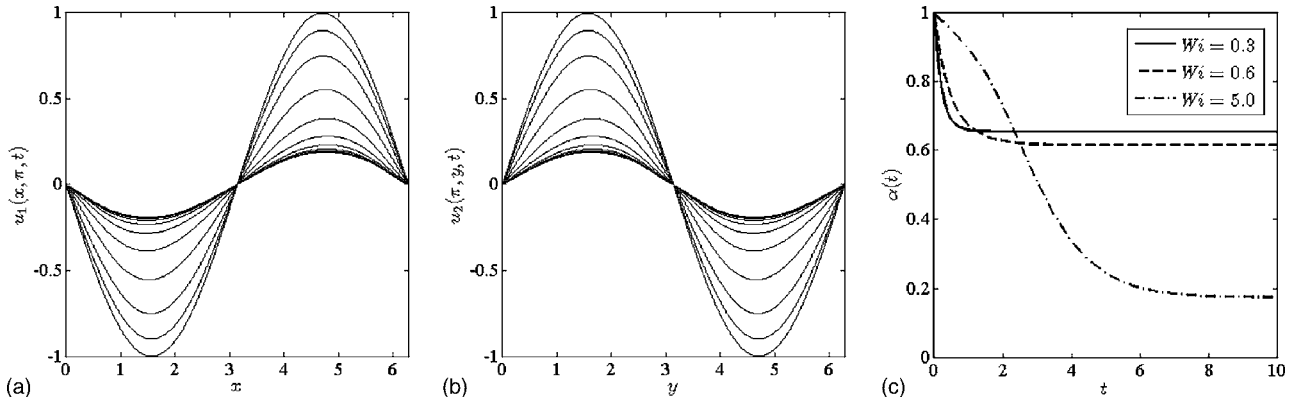

FIG. 3. (a) The velocity $u_1(x,\pi,t)$ for $\mathcal{W}i=5.0$ for $t=0,1,\ldots,10$. The initial data are $u_1(x,\pi,0)=-\sin x$ and u_1 decreases in time (from $t=0$ to 10) to a nearly steady solution. (b) $u_2(\pi,y,t)$ for $t=1,2,\ldots,10$ decreasing to a nearly steady solution. (c) The strain rate at the central hyperbolic point, $\alpha(t)=\partial\mathbf{u}/\partial x(\pi,\pi,t)$ for $\mathcal{W}i=0.3$ (solid line), 0.6 (dashed line), and 5.0 (dotted line).

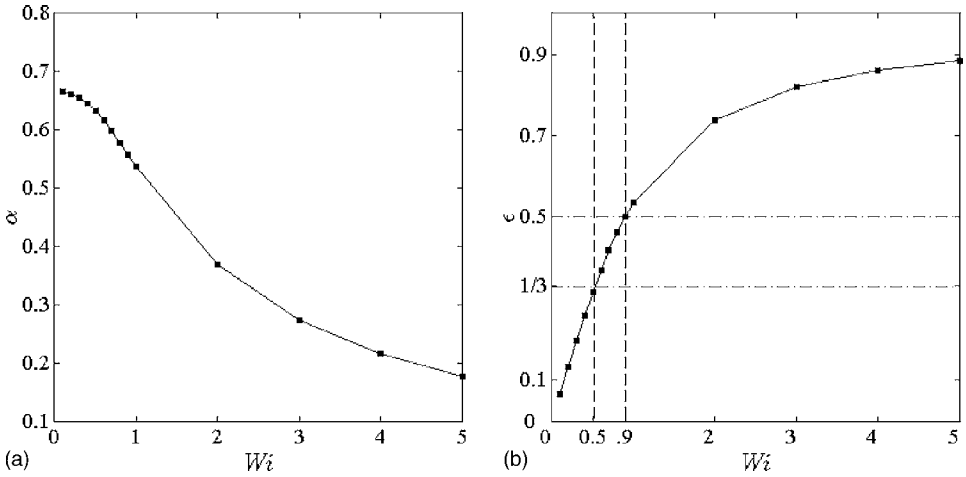

FIG. 4. (a) The "large-time" strain rate $\alpha=\partial\mathbf{u}/\partial x(\pi,\pi)$ at the central hyperbolic point. α at steady state decreases as a function of $\mathcal{W}i$. (b) The effective Weissenberg number $\epsilon=\alpha\mathcal{W}i$ plotted as a function of $\mathcal{W}i$, from computed values of α; $\epsilon_1=1/3$ corresponds to $\mathcal{W}i_1\approx0.5$ and $\epsilon_2=1/2$ corresponds to $\mathcal{W}i_2\approx0.9$.

the other components of the stress tensor as well. For example, the analogous solution for S_{22} is given by

$$\frac{1}{1+2\epsilon}+e^{-(1+2\epsilon)t}H_{22}(xe^{-\epsilon t},ye^{\epsilon t}),$$

and proceeding as was done for S_{11}, it suggests that

$$S_{22,\infty}\sim\frac{1}{(1+2\epsilon)}+|y|^{q'}, \tag{13}$$

with $q'=1/\epsilon+2$. Finally, the local solution for S_{12} has the form

$$e^{-t}H_{12}(xe^{-\epsilon t},ye^{\epsilon t}).$$

The purpose of the next section will be to summarize our numerical results and in particular to compare the numerical solutions to the approximate solution we have discussed. We will demonstrate that the approximate solution does an excellent job of capturing the singular behavior of the solution, particularly for S_{11}, at the central hyperbolic point.

IV. NUMERICAL RESULTS

The critical Weissenberg numbers obtained in Sec. III were $\mathcal{W}i_1\approx0.5$ and $\mathcal{W}i_2\approx0.9$. We first consider the dynamics for three values of $\mathcal{W}i$ (0.3, 0.6, and 5.0) at a fixed time $t=6$, after evolving from initial data $\mathbf{S}(0)=\mathbf{I}$. These values are chosen to sit between transitions in the singular structure of the solution as $\mathcal{W}i$ is increased. We note here that although we scaled time as $\mathcal{W}i\cdot t$ for the local solution, everything that follows will be in the unscaled time, and when we compare the simulations with the local solution, we will make the necessary adjustments. Figure 1 shows contour plots of the vorticity ω at $t=6$ for these three values of $\mathcal{W}i$. For the lower Weissenberg numbers, the vorticity for the Stokes flow is not changed qualitatively by the addition of the polymer stress field, i.e., the four-vortex flow persists and no additional features are created. Above a critical Weissenberg number this begins to change, and we see for $\mathcal{W}i=5.0$ that additional oppositely signed vortices are generated along the stable and unstable manifolds of the hyperbolic point. Increasing the Weissenberg number decreases the overall magnitude of vortex strength.

Figures 2(a)–2(c) show contour plots of tr$\mathbf{S}$ at $t=6$. At the central hyperbolic point, tr$\mathbf{S}$ is dominated by S_{11}. For $\mathcal{W}i=0.3$ and 0.6, the solution has essentially relaxed to a bounded steady state by this time. This is not so for $\mathcal{W}i=5.0$, which appears to be diverging to an unbounded state. The stress field grows rapidly near the hyperbolic points in the flow and concentrates along the unstable manifold of the hyperbolic point; see Fig. 2(c). The stress accumulates on elliptical "stress islands" whose magnitude grows in $\mathcal{W}i$ while concentrating on thinner and thinner sets in the plane. At this time, the high wave-number part of the spectrum remains bounded above by 10^{-8}. The shear stress component S_{12} likewise shows transitions in its spatial structure with $\mathcal{W}i$, but remains much smaller in magnitude; see Figs. 2(d)–2(f). Figures 2(g)–2(i) show contour plots of the first component of the force due to polymer stress at $t=6$: $F_1=\partial_x S_{11}+\partial_y S_{12}$ (due to symmetries, the second component is a $\pi/2$ rotation of the first). The forces are of much smaller magnitude than the stress components; the large gradients that make up the stress islands in Fig. 2(c) ($\partial_y S_{11}$ and $\partial_x S_{22}$) are not components of the force $\nabla\cdot\mathbf{S}$. It is interesting to note that the only appearance of $\partial_y S_{11}$ ($\partial_x S_{22}$) in Eq. (2) is in the advection term of S_{11} (S_{22}).

Figures 5(a)–5(c) show the stress $S_{11}(\pi,y)$ at $t=6$, i.e., slices along the stable manifold about the hyperbolic point, ranging in $\mathcal{W}i$ from 0.1 to 0.5 (a), 0.6 to 0.9 (b), and 1.0 to 5.0 (c). By this time, the stress has begun to concentrate at the central hyperbolic point, but for $\mathcal{W}i\lesssim0.5$ these profiles appear smooth. The first transition appears to occur at $\mathcal{W}i_1\approx0.5$, above which the stress remains bounded, but appears to approach a cusp singularity in time. Above $\mathcal{W}i_2\approx0.9$, the maximum of the stress appears to become unbounded in time.

Our computations suggest the emergence of a singular algebraic structure of the form $S_{11}(\pi,\pi-y)\sim|y|^q$, near the central hyperbolic point, where q is a function of $\mathcal{W}i$. In order to make this more rigorous, we analyze the structure of $\hat{S}_{11}(\pi,k)$, the Fourier transform (in y) of $S_{11}(\pi,y)$, shown for $\mathcal{W}i=0.6$ and $\mathcal{W}i=2.0$ in Figs. 6(a) and 6(d). Consistent with the emergence of a singular structure, $\hat{S}_{11}(\pi,k)$ decays less rapidly (in k) as time progresses. To analyze the structure of

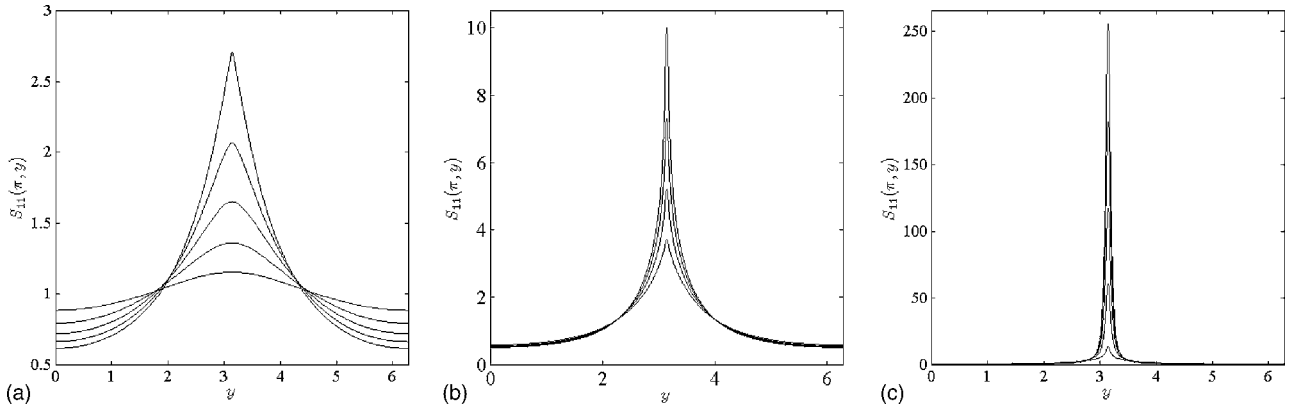

FIG. 5. $S_{11}(\pi,y)$ at $t=6$ for (a) $\mathcal{W}i=0.1-0.5$, (b) $\mathcal{W}i=0.6-0.9$, and (c) $\mathcal{W}i=1-5$.

the singularity, we make the ansatz that $|\hat{S}_{11}(\pi,k)| \sim Ae^{-\delta k}k^{-(q+1)}(1+C/k)$ for $|k|\gg 1$. This is motivated by Laplace's method for expressing the asymptotic decay of a one-dimensional Fourier series (for an analytic function) in terms of the distance and algebraic structure of the nearest singularity to the real axis. This method has been used in many numerical studies of singularity formation (see, e.g., Refs. 22–24). The value of δ gives the distance of the singularity to the real axis and q gives its algebraic order. Given the consistency of the computed spectra with this ansatz, the emergence of the singularity of the form $|y|^q$ is associated with the approach of δ to zero in time. We fit $|\hat{S}_{11}(\pi,k)|$ to this ansatz over successive quadruples $(k,k+1,k+2,k+3)$ and use Newton's method to find pointwise estimates for A, δ, q, and C. These fits for $\mathcal{W}i=0.6$ and 2.0 are shown in Figs. 6(b), 6(c), 6(e), and 6(f). It is typical that the range in k over which one finds smooth fits in k is limited by attempting to pick out an asymptotic decay structure from a solution made increasingly inaccurate by the oncoming singularity (see Ref. 24).

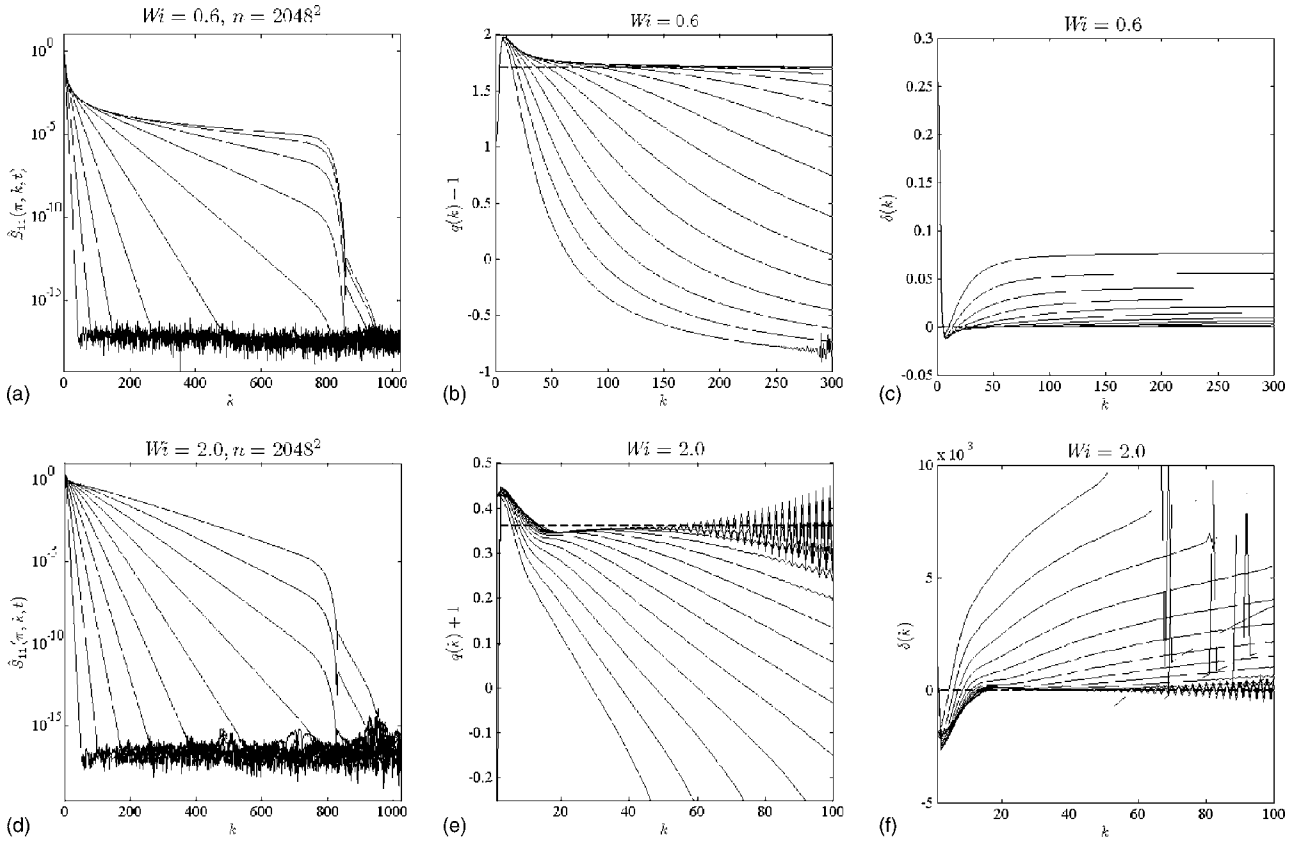

FIG. 6. (a) $\hat{S}_{11}(\pi,k)$ for $\mathcal{W}i=0.6$ and $t=1,2,\ldots,10$. The spectrum decays less rapidly as time progresses. (b) For $\mathcal{W}i=0.6$ and at the same times, the fit for q in the ansatz $|\hat{S}_{11}(k)|\sim Ae^{-\delta k}k^{-(q+1)}(1+C/k)$. As time progresses, the value $q\approx 0.7$ is approached for a wide range of wave numbers. The dashed line represents the value $(1-2\epsilon)/\epsilon+1$ corresponding to $\mathcal{W}i=0.6$. (c) The corresponding fit to δ in the ansatz. As time progresses, the value $\delta=0$ is approached for a wide range of wave numbers. (d)–(f) Same as (a)–(c) for $\mathcal{W}i=2.0$; in this case $q\approx -0.65$.

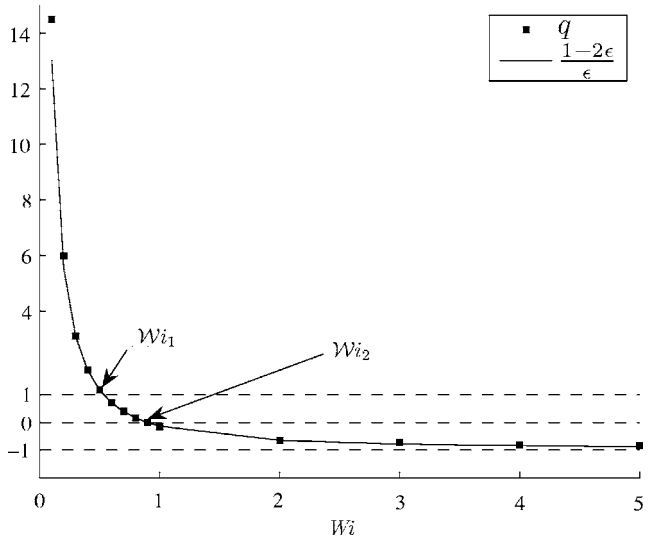

FIG. 7. The solid points are estimates of q as obtained from the spectral analysis. They correspond to the solution approximation of the form $|y|^q$. The solid curve is $(1-2\epsilon)/\epsilon$, as computed from the local solution of Sec. III. The excellent agreement indicates that the local approximation matches the simulations quite well.

For all Weissenberg numbers, our computations suggest $\delta \to 0$ in time, and hence the algebraic structure of the solution becomes progressively more pronounced. The data points in Fig. 7 show the fit exponent q versus the Weissenberg number. We find that q and hence the smoothness of the solution depends sensitively on the Weissenberg number. For $\mathcal{W}i \lesssim \mathcal{W}i_1$, this exponent q is greater than 1, hence the solutions have at least one continuous derivative. The first transition occurs at $q=1$. Between $\mathcal{W}i_1$ and $\mathcal{W}i_2$, the solutions are cusps, bounded but with a singularity in the first derivative, as $0<q<1$. At $\mathcal{W}i=\mathcal{W}i_2$, this singularity becomes unbounded as q becomes negative. The exponent $(1-2\epsilon)/\epsilon$ in the local solution γ_∞ from Eq. (12) is compared with the computed exponents q in this figure as well. The comparison is quite good for the range of Weissenberg numbers. Note that the exponent q appears to remain bounded below by -1, implying that although the stress components are becoming unbounded, they remain integrable. This is supported by Eq. (5), which implies that tr**S** remains integrable as long as the input power is bounded. Our computations confirm that the input power does indeed remain bounded as does the strain energy, which the bound given in Eq. (6) implies.

We now turn to examining the temporal structure of the stress field. Figures 8(a)–8(f) show slices of the stress S_{11} along both the stable and unstable directions around the hyperbolic point at (π,π) for $t=1,2,\ldots,10$ for our three example Weissenberg numbers. In the preceding section, we derived a local solution about the hyperbolic point. Our simulations and this local solution suggest the local form

$$S_{11}(x,y-\pi,t) \approx \bar{S}(\mathcal{W}i) + e^{P(\mathcal{W}i)t} H(y e^{Q(\mathcal{W}i)t}), \tag{14}$$

where the exponential rate, P, is negative for $\mathcal{W}i<\mathcal{W}i_2$, indicating a bounded solution, and P is positive for $\mathcal{W}i>\mathcal{W}i_2$, where the solutions are diverging. The collapsing in-

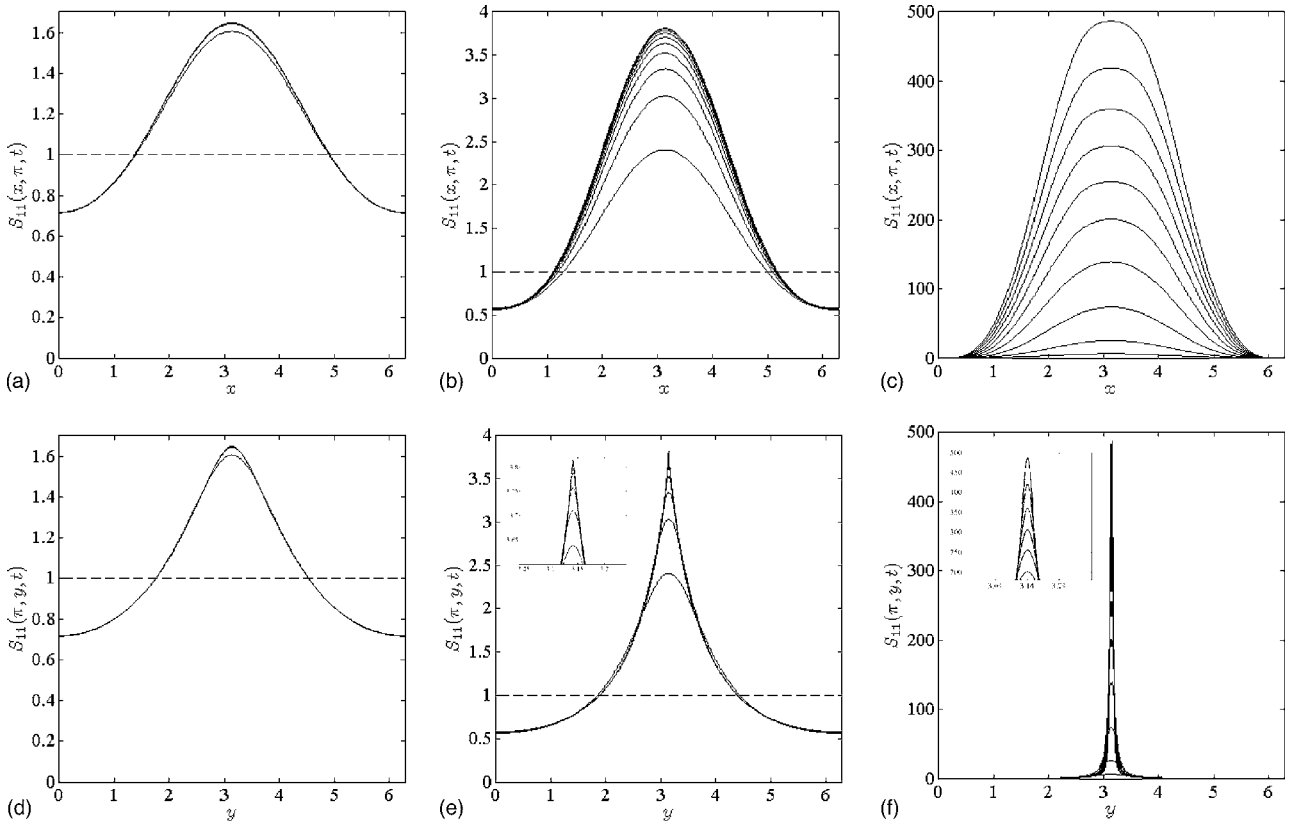

FIG. 8. (a)–(c) $S_{11}(x,\pi)$ for $t=1,2,\ldots,10$, increasing in time for $\mathcal{W}i=0.3$, 0.6, and 5.0, respectively. (d)–(f) $S_{11}(\pi,y)$ for $t=1,2,\ldots,10$, increasing in time for $\mathcal{W}i=0.3$, 0.6, and 5.0, respectively.

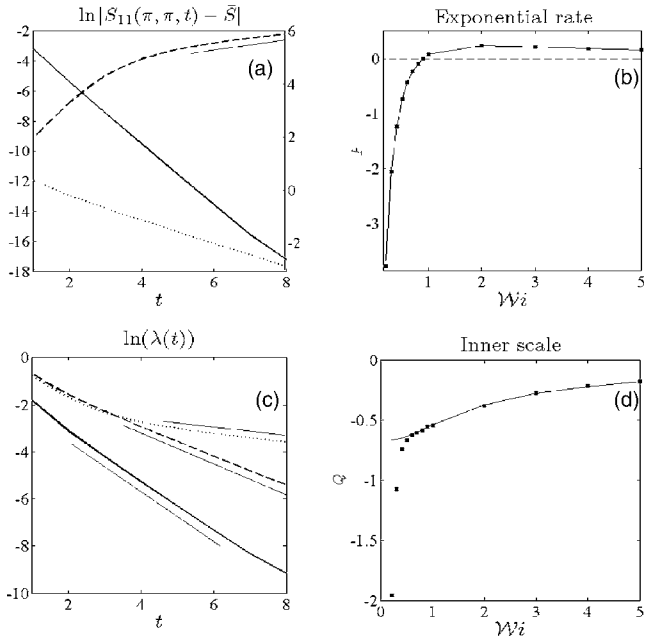

FIG. 9. (a) $\ln(|S_{11}(\pi,\pi,t)-\bar{S}|)$: The solid curve is for $\mathcal{W}i=0.3$ (scale left axis), the dotted curve is for $\mathcal{W}i=0.6$ (scale right axis), and the dashed curve is for $\mathcal{W}i=5.0$ (scale right axis). The curves are approximately linear after some time giving an exponential rate of convergence toward (negative slope) or divergence from (positive slope) $\bar{S}$. The slope for each $\mathcal{W}i$ gives the exponential rate $P(\mathcal{W}i)$. (b) The exponential rate P plotted vs $\mathcal{W}i$. The curve is $(2\epsilon-1)/\mathcal{W}i$, as computed from the local solution of Sec. III (all figures are in unscaled time). (c) $\ln(\lambda(t))$ for $\mathcal{W}i=0.3$ (solid curve), $\mathcal{W}i=0.6$ (dotted curve), and $\mathcal{W}i=5.0$ (dashed curve). For $\mathcal{W}i=0.3<\mathcal{W}i_1$, the second derivative at the hyperbolic point is not diverging and the curve levels off as the peak value is approached. For $\mathcal{W}i>\mathcal{W}i_1$, the curves are approximately linear after some time, indicating an exponentially collapsing inner scale. The slope for each $\mathcal{W}i$ gives the collapse rate $Q(\mathcal{W}i)$. (d) The inner scale Q is plotted vs the Weissenberg number. The solid curve is $-\epsilon/\mathcal{W}i$, as computed from the local solution of Sec. III.

ner scale Q is always positive. Hence, the exponential rate P controls the rate of convergence (divergence) toward (from) $\bar{S}$, and e^{-Qt} defines a collapsing inner scale of the local solution. The local solution suggests that $\bar{S}=1/(1-2\epsilon)$, $P(\mathcal{W}i)=(2\epsilon-1)/\mathcal{W}i$, and $Q(\mathcal{W}i)=\epsilon/\mathcal{W}i$, and we will compare these values with the values we obtain from the simulations.

When the solution appears to remain bounded (i.e., $\mathcal{W}i<\mathcal{W}i_2$), $\bar{S}=1/(1-2\epsilon)$ is an excellent predictor for the long-time value of $S_{11}(\pi,\pi,t)$. In fact, for $\mathcal{W}i=0.1$ the difference is $\mathcal{O}(10^{-14})$. Therefore, to compute P from the simulations, we consider $|S_{11}(\pi,\pi,t)-\bar{S}|$. This will give us the rate at which the solution is approaching or diverging from this value. The logarithm of this difference is plotted in Fig. 9(a). These curves appear linear (after $t\approx 5$ for $\mathcal{W}i=5.0$) suggesting an exponential rate. For $\mathcal{W}i<\mathcal{W}i_2$, the peak value, $\bar{S}$, is approached exponentially in time, and for $\mathcal{W}i>\mathcal{W}i_2$, the maximum of the stress is repelled from $\bar{S}$ exponentially in time. Figure 9(b) shows this rate, P, versus $\mathcal{W}i$. When $\mathcal{W}i>\mathcal{W}i_2$, this approach rate becomes positive, and though it is initially increasing in $\mathcal{W}i$, it eventually begins to decrease for $\mathcal{W}i\gtrsim 2.0$. Previously we have seen that as $\mathcal{W}i$ is increased, the singular solution has an exponent approaching -1 (see Fig. 7) making the solution more difficult to resolve near the hyperbolic point. However, the rate at which the singularity is being approached is decreasing in $\mathcal{W}i$ (for $\mathcal{W}i\gtrsim 2.0$). The underlying smooth curve is the predicted exponential approach rate $P(\mathcal{W}i)=(2\epsilon-1)/\mathcal{W}i$. We see that the local solution does a good job predicting this approach rate.

The local solution Eq. (12) also predicts an inner scale, or a collapsing length scale, which is so apparent in Fig. 8. The local solution predicts that the scale looks like $e^{-\epsilon t/\mathcal{W}i}=e^{-\alpha t}$. To identify this scale in the simulations [referred to as $Q(\mathcal{W}i)$], we construct the length scale

$$\lambda(t)=\left(\frac{|S_{11}(\pi,\pi,t)-\bar{S}|}{|\partial_{yy}S_{11}(\pi,\pi,t)|}\right)^{1/2}. \tag{15}$$

λ measures the ratio of the rate at which $S_{11}(\pi,\pi,t)$ approaches (or diverges from) $\bar{S}$, over the rate at which the second derivative is diverging at the central hyperbolic point (at least for $\mathcal{W}i>\mathcal{W}i_1$). Figure 9(c) shows the logarithm of λ for $\mathcal{W}i=0.3$, 0.6, and 5.0. The slope of λ is the exponential rate of collapse $Q(\mathcal{W}i)$. These curves appear linear (after $t\approx 5$ for $\mathcal{W}i=5.0$) suggesting an exponential rate. Figure 9(d) shows Q as a function of the Weissenberg number. The inner scale is collapsing for all $\mathcal{W}i>\mathcal{W}i_1$, and the rate of collapse is decreasing in the Weissenberg number. In Fig. 9(d), we also plot the predicted scaling rate $-\alpha$, which compares well with the computed rate for $\mathcal{W}i>\mathcal{W}i_1$. We do not expect the inner scale to have meaning for $\mathcal{W}i<\mathcal{W}i_1$, because for these solutions the singularities are higher order and the second derivatives are not diverging.

We turn now to the comparison of the simulation with the local solution for the other components of the stress tensor. The local solution suggests that $S_{12}(x,y,t)\sim e^{-t}H_{12}(xe^{-\epsilon t},ye^{\epsilon t})$ and indeed symmetry dictates that $S_{12}=0$ at the central hyperbolic point.

We now compare our numerically computed solution for S_{22} with the predictions of the local model. Our simulations suggest that S_{22} remains bounded, and indeed Eq. (13) predicts that S_{22} will go to a constant $1/(1+2\epsilon)$, which is bounded for all ϵ. This comparison is excellent for S_{22}; see Fig. 10(a). However, the local solution has a time asymptotic structure $|y|^{q'}$, with $q'=2+1/\epsilon$. When we make the spectral ansatz $|\hat{S}_{22}(\pi,k)|\sim A'e^{-\delta' k}k^{-(q'+1)}(1+C'/k)$ and fit q', it compares well with an exponent of the form $q'=1/\epsilon$; see Fig. 10(b). It is unclear what this discrepancy is stemming from. It is possible that the less singular solutions for S_{22} are harder to fit to the ansatz. Again the distance from the singularity to the real axis, δ', goes to zero for all Weissenberg numbers, and in fact, $\delta'\approx\delta$, i.e., the singularity for S_{11} is approached at the same rate as the singularity for S_{22}.

We finish this section by a further comment about the forces due to the polymer stress. As we observed, the most singular terms in the stress are $\partial_y S_{11}$ (and by symmetry $\partial_x S_{22}$). These components do not enter into the force in the momentum balance equations. The polymer forces $\nabla\cdot\mathbf{S}$ remain relatively small near the central hyperbolic point, although they do grow linearly, rather than exponentially, along the incoming and outgoing streamlines. Following a referee's suggestion, we further analyzed the data for S_{11} beyond the second critical Weissenberg number and observe

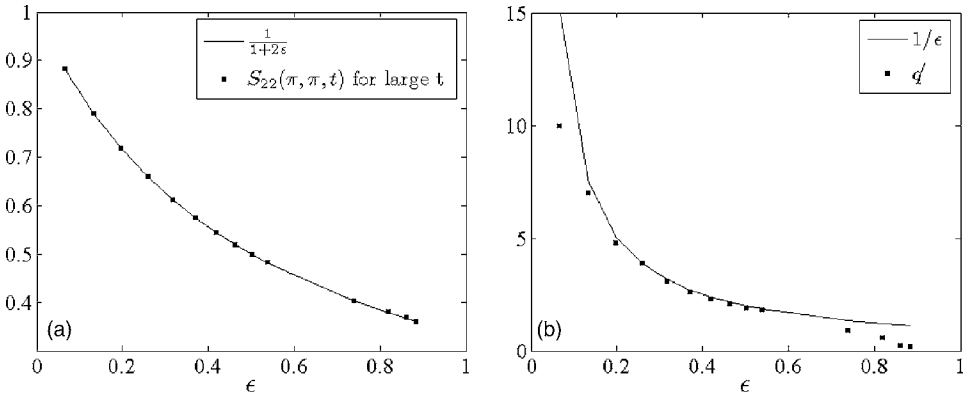

FIG. 10. (a) For S_{22}, a comparison of the constant term of the local solution, $1/(1+2\epsilon)$, with the "large time" converged value of $S_{22}(\pi,\pi,t)$. (b) For S_{22}, a comparison of a possible exponent, $1/\epsilon$, with the exponent q' estimated from the Fourier spectra.

that the singular stress S_{11} reaches an approximate steady state outside a small region around the outgoing streamlines. This is approximately when $\epsilon t > \ln(1/|y|)$. There is a small region near the stagnation streamline $|y| < e^{-\epsilon t}$ where the stress is growing exponentially, $S_{11} \propto e^{(2\epsilon-1)t}$. The net force from this unsteady region decreases in time, and hence the unsteady region has a decreasing effect on the flow. In Fig. 11, we plot

$$\int\int_{R(t)} |S_{11}| dxdy, \quad \text{with } R(t) = [0,2\pi] \times [0,e^{-\alpha t}]$$

over time and see that although the stress in the region $R(t)$ is initially increasing, it begins to decrease rapidly after $t \approx 5$ This appears to explain how the extension rate at the stagnation point approaches a steady value while the stress on the stagnation streamline is still growing exponentially.

We have thus far focused our attention exclusively on the central hyperbolic point, but it is important to note that the singularity we observed in the stress field actually appears to occur as a line singularity along the outgoing streamline. We analyzed the structure of the solution at points along this line and observe that the singular structure persists in an interval about the hyperbolic point.

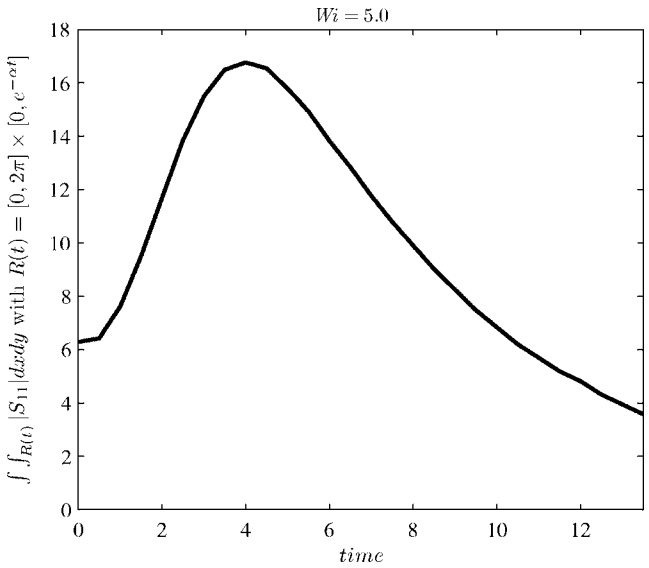

FIG. 11. The integral $\int\int_{R(t)} |S_{11}|(x,y)\, dx\, dy$ with $R(t)=[0,2\pi]\times[0,e^{-\alpha t}]$ for $\mathcal{W}i=5.0$.

V. OTHER CONSIDERATIONS

The observed singularities depend sensitively on many aspects of the problem besides the bare Weissenberg number. For example, we have found that adding a higher-order harmonic to the background force will change $\alpha(\mathcal{W}i)$ and hence the order of the singularity. The choice of $\beta \cdot \mathcal{W}i$ also affects α. We also ran simulations for the case $\beta \cdot \mathcal{W}i = 1$. For a fixed $\mathcal{W}i$, increasing the constant C, with $\beta \cdot \mathcal{W}i = C$, increases β, and this yields a further decrease in the strain rate α. This leads to a reduction in the order of the singularity (both predicted and observed in simulations); for example, if $\mathcal{W}i = 0.6$, the exponent predicted by the local solution and computed in the simulation for $C = 1/2$ is $q \sim 0.7$, whereas for $C = 1$, $q \sim 1.6$.

We have also investigated the robustness of the singularity to dynamical changes in the Weissenberg number. For example, we took our initial data from a well-resolved but near-cusp solution with $\mathcal{W}i = 0.6$, and proceeded to run a simulation with this data but using instead $\mathcal{W}i = 0.2$. Figure 12(a) shows that the solution rapidly relaxes to what appears to be the typical solution for $\mathcal{W}i = 0.2$. The maximum decreases in time and the solution reaches near steady state. As time proceeds, the spectrum [say $\hat{S}_{11}(\pi,k)$] shows an evolution toward more rapid decay, indicating that the solution is becoming *less* singular in time. Recall that the algebraic

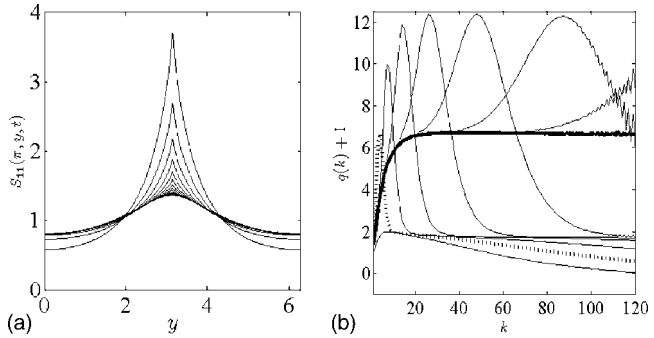

FIG. 12. (a) For $\mathcal{W}i = 0.2$, the stress component $S_{11}(\pi,y)$ for $t = 0,1,\ldots,10$ (amplitude decreases in time). Initial data come from near-cusp solutions with $\mathcal{W}i = 0.6$. (b) Fit to q in the spectral ansatz. Time progresses from the heavy dotted line to the heavy solid line. Initially the fit $q \sim 0.7$ (indicating a cusp) is dominant, but as time progresses the line $q \sim 5.5$ becomes dominant (indicating an increase in smoothness of the solution).

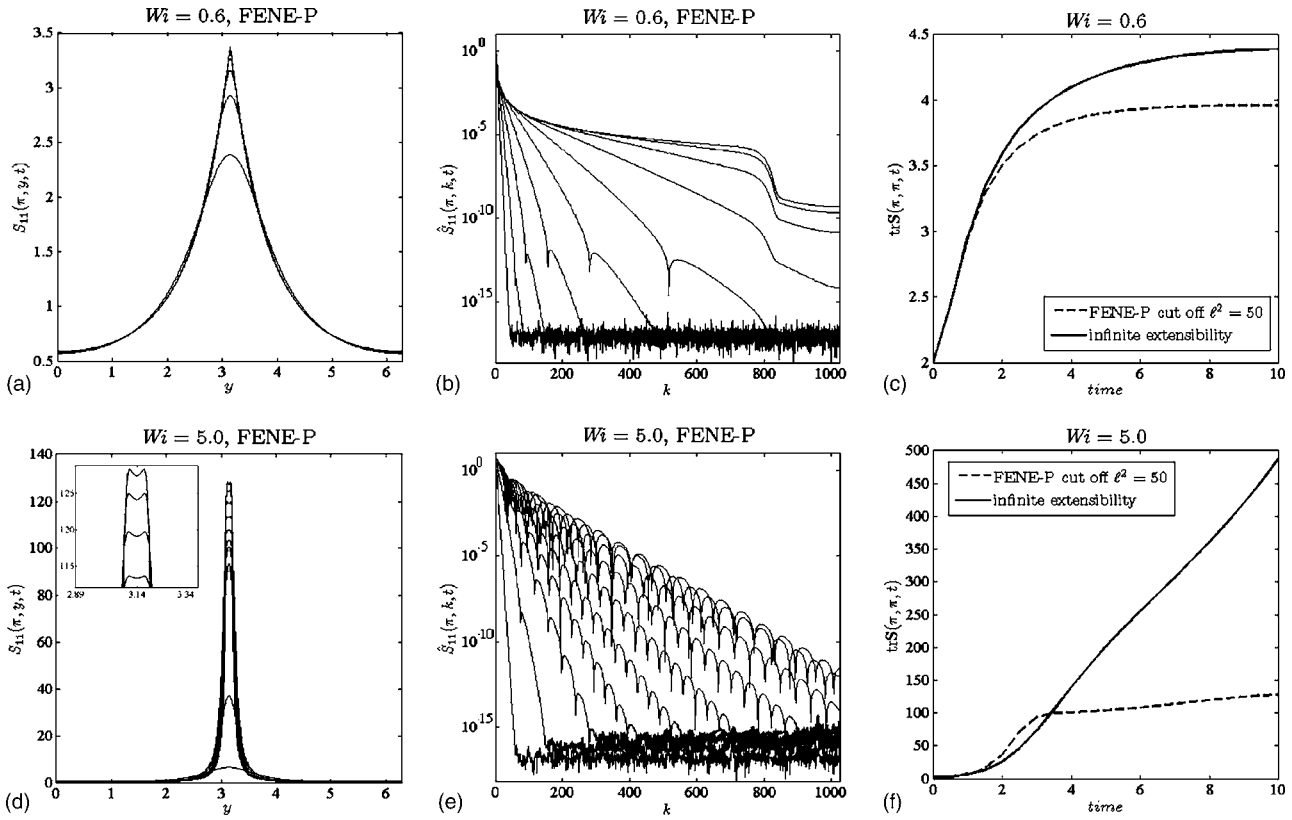

FIG. 13. (a) Plots of $S_{11}(\pi,y,t)$, with FENE-P penalization, increasing in time to cusplike solution for $\mathcal{W}i=0.6$. (b) Comparison of $\mathrm{tr}\mathbf{S}(\pi,\pi,t)$ with FENE-P penalization (dotted line) and without the FENE-P penalization (solid line) for $\mathcal{W}i=0.6$. (c) Plots of $S_{11}(\pi,y,t)$, with FENE-P penalization, increasing in time to cusplike solution for $\mathcal{W}i=2.0$. (d) Comparison of $\mathrm{tr}\mathbf{S}(\pi,\pi,t)$ with FENE-P penalization (dotted line) and without FENE-P penalization (solid line) for $\mathcal{W}i=2.0$.

structure is approximated as $|y|^q$, where $q=(1-2\epsilon)/\epsilon$. For $\mathcal{W}i=0.2$, $q\approx 5.5$, and for $\mathcal{W}i=0.6$, $q\approx 0.7$. We use the same method as in Sec. IV to fit the exponent with these data, and $q(k)+1$ is plotted in Fig. 12(b). Initially the fit gives $q(k)\sim 0.7$, which indicates a cusp. As time progresses, the fit appears to give $q\sim 0.7$ for lower wave numbers and $q\sim 5.7$ for higher wave numbers. By $t=10$, the fit appears to give $q\sim 5.7$ for all wave numbers (where convergence is seen). This seems to suggest that initially the more dominant singularity has $q=0.7$, which agrees well with $\mathcal{W}i=0.6$, and then as time progresses this singularity diminishes and the singularity with $q=5.7$, corresponding to $\mathcal{W}i=0.2$, becomes more dominant.

The Oldroyd-B equations are often criticized for allowing infinite extensibility of polymer chains. Indeed, those singular solutions with $\mathcal{W}i>\mathcal{W}i_2$ correspond to arbitrarily large extension. Still, we have also found a whole spectrum of solutions with finite extension that are singular nonetheless. To understand whether the singularities we have observed are due to this infinite extensibility, we add a FENE-P cutoff to our model.[25] The Stokes–Oldroyd-B equations with the FENE-P penalization are given by

$$-\nabla p+\Delta\mathbf{u}=-\beta\nabla\cdot\mathbf{S}+\mathbf{f}\quad\text{and}\quad\nabla\cdot\mathbf{u}=0,$$

$$\partial_t\mathbf{C}+\mathbf{u}\cdot\nabla\mathbf{C}-(\nabla\mathbf{u}\mathbf{C}+\mathbf{C}\nabla\mathbf{u}^T)+\frac{1}{\mathcal{W}i}(\mathbf{S}-\mathbf{I})=0,$$

$$\mathbf{S}=\frac{\mathbf{C}}{1-\left(\mathrm{tr}\,\mathbf{C}/\ell^2\right)},$$

where ℓ represents the ratio of the maximum polymer length to the length of the polymer when coiled. In what follows, we use $\ell^2=50$. We consider two cases, $\mathcal{W}i_1<\mathcal{W}i<\mathcal{W}i_2$ and $\mathcal{W}i>\mathcal{W}i_2$.

First we consider $\mathcal{W}i=0.6$. Figure 13(a) shows slices of $S_{11}(\pi,y)$ for $t=0,1,\ldots,10$. The solution appears to be approaching a cusp singularity quite similar to that of $\mathcal{W}i=0.6$ without the FENE-P penalization; see Fig. 8(e). Figure 13(c) shows the value of $\mathrm{tr}\mathbf{S}(\pi,\pi,t)$ for $\mathcal{W}i=0.6$ both with and without the FENE-P penalization. We see that the penalization reduces the maximum value of the stress, but in this range of $\mathcal{W}i$, the maximum value is bounded even without the penalization, and the differences are minimal. The strain rate α is decreased by the polymer stress field, but is about 3% larger than for the case without the FENE-P penalization. Figure 13(b) show the Fourier spectrum, $\hat{S}_{11}(\pi,k)$ for $t=1,\ldots,10$. The early time spectrum ($t<6$) shows an oscillation that eventually moves out to higher and higher wave numbers. We will comment more on this for $\mathcal{W}i=5.0$, but this likely indicates that the singularity is changing form. An oscillation of this form is consistent with having two, rather than one, singularities propagating toward the real axis, and the loss of the oscillation suggests their merger into a single

singularity as the axis is approached. If we fit the spectrum to the original ansatz, we obtain an exponent $q \approx 1.0$ indicating that it may still have a cusplike nature, although the FENE-P penalization has increased the exponent. In summary, the FENE-P penalization does not appear to smooth out the cusp and hence any difficulties in numerical simulations related to the large gradients in the stress field at the central hyperbolic point will still be apparent.

For $\mathcal{W}i > \mathcal{W}i_2$, the FENE-P penalization does keep tr$\mathbf{S}$ bounded. For $\mathcal{W}i = 5.0$, Fig. 13(d) shows slices of $S_{11}(\pi, y)$ for $t = 0, 1, \ldots, 10$, and Fig. 13(f) shows tr$\mathbf{S}(\pi, \pi, t)$ for $\mathcal{W}i = 5.0$ with and without the FENE-P penalization. Again, the FENE-P penalization appears to cause a different type of approaching singularity to form in this case. Instead of a single cusp or an infinite singularity, the solution appears to have bifurcated at the tip. This can be seen on the Fourier transform side as well. Figure 13(e) shows an oscillatory spectrum. This indicates a pair of singularities. The distance between these oscillations (Δk) is related to the distance between the singularities (Δy). In this case we have $\Delta y = \pi/\Delta k \approx \pi/45 \approx 0.07$. This compares well with the separation between the two apparent singularities in S_{11}.

Although these results are not conclusive, it does appear that at least a simple FENE-P penalization will not resolve all of the difficulties associated with the Oldroyd-B equations, and that allowing infinite extensibility in polymer chain lengths is not at the root of all difficulties with these equations. We suspect that FENE may suffer from similar difficulties.

VI. CONCLUSION

The behavior and smoothness of solutions to the Stokes–Oldroyd-B equations is very sensitive to the Weissenberg number. Nearly singular structures in the stress field arise at every Weissenberg number. We observe two dramatic transitions that for our simulations occur for $\mathcal{W}i_1 \approx 0.5$ and $\mathcal{W}i_2 \approx 0.9$. The first, at $\mathcal{W}i_1 \approx 0.5$, is distinguished by the appearance of a cusp singularity in the stress field that is approached exponentially in time at the central hyperbolic point in the flow. Below this critical Weissenberg number, although one or more derivatives of the stress may be bounded, the solutions are still approaching a singular solution. At higher Weissenberg number (beyond $\mathcal{W}i_2 \approx 0.9$), the singular structures that are approached are unbounded at the central hyperbolic point.

The constructed local solution agrees quite well with the numerical results giving similar dependence on $\mathcal{W}i$ for regularity of solutions, exponential rates, and inner scaling. The constructed local solution also introduces the parameter ϵ, the "effective" Weissenberg number. The nature of the singularity depends critically on ϵ, which includes of course the Weissenberg number but also the local strain rate of the flow at the hyperbolic point, α. Currently, we determine α with our simulations, however it should be possible to solve for α in general by matching the inner and outer flow conditions. This is a complicated problem but well worth studying. One way to attempt this might be to consider wave-number limited velocities (see Fig. 3). As our method involves a spectral code, we were able to check this to some degree. We solved the system keeping only the first few modes of $\mathbf{u}$ ($k \leqslant 4$). In these simulations, we observed that the convergence of α was similar to that of the full solution. The flow rate goes to a steady state rapidly (and on a time scale similar to that for the full solution) but the converged value of α in the wave-number limited case was slightly higher than for the full solution. We have not pursued this idea further, but believe that it might be one way to consistently solve for the flow rate.

An interesting point to reiterate is the fact that although there is significant evidence that for $\mathcal{W}i > \mathcal{W}i_1$ first derivatives of the stress are growing exponentially fast, these very large derivatives are not components of the polymer stress, and hence do not directly feed back into the Stokes equation. One might be able to use this fact to obtain bounds on the stress that in turn yield bounds on $\mathbf{u}$ to show that the solutions (although exponentially large) remain bounded for all time.

It may be that these emerging singularities lie at the root of many difficulties in numerical simulations of viscoelastic fluids using the Oldroyd-B model. There is a vast literature regarding the "high Weissenberg" number problem; see Ref. 26, Chap. 7 for a careful exposition of many relevant results. It appears that the solution to the Oldroyd-B equations in any flow that contains a hyperbolic stagnation point will develop large stress gradients at an exponential rate, even for a Weissenberg number much lower than those related to the infinite extension of polymer chains. However, we only observe this singular behavior for a pure extensional flow; more general flows may not demonstrate these properties. These large stress gradients (due to the cusp singularity) will be present even with a restriction on the length of the polymer chains. We have added a simple FENE-P penalization to our numerical simulation and observe that for $\mathcal{W}i < \mathcal{W}i_2$ there is still an exponential approach to a cusp singularity, and for $\mathcal{W}i > \mathcal{W}i_2$, although tr$\mathbf{S}$ is bounded, there remains an approach to a singularity, although the type is not quite as clear. Many of these difficulties would be alleviated if not eliminated by incorporating a scale-dependent dissipation (e.g., diffusion) into the stress advection, see for example Refs. 27 and 28.

ACKNOWLEDGMENTS

The authors would like to thank Estarose Wolfson at the Courant Institute for porting our spectral code to the NYU MAX cluster. We would also like to thank John Hinch for useful comments on our work. The first author was partially supported by NSF Grant No. DMS-0600668. The second author was partially supported by DOE Grant No. DE-FG02-88ER25053. Finally, the authors would like to thank the referees for very constructive comments.

[1] A. Groisman and V. Steinberg, "Elastic turbulence in a polymer solution flow," Nature **405**, 53 (2000).
[2] A. Groisman and V. Steinberg, "Efficient mixing at low Reynolds numbers using polymer additives," Nature **410**, 905 (2001).
[3] A. Groisman and V. Steinberg, "Elastic turbulence in curvilinear flows of polymer solutions," New J. Phys. **6**, 29 (2004).
[4] P. E. Arratia, C. C. Thomas, J. Diorio, and J. P. Gollub, "Elastic instabili-

ties of polymer solutions in cross-channel flow," Phys. Rev. Lett. **96**, 144502 (2006).
[5]J. M. Rallison and E. J. Hinch, "Do we understand the physics in the constitutive equation?" J. Non-Newtonian Fluid Mech. **29**, 37 (1988).
[6]O. G. Harlen, J. M. Rallison, and M. D. Chilcott, "High-Deborah-number flows of dilute polymer-solutions," J. Non-Newtonian Fluid Mech. **34**, 319 (1990).
[7]O. G. Harlen, "High-Deborah-number flow of a dilute polymer-solution past a sphere falling along the axis of a cylindrical tube," J. Non-Newtonian Fluid Mech. **37**, 357 (1990).
[8]O. G. Harlen, E. J. Hinch, and J. M. Rallison, "Birefringent pipes: The steady flow of a dilute polymer solution near a stagnation point," J. Non-Newtonian Fluid Mech. **44**, 229 (1992).
[9]R. G. Larson, *The Structure and Rheology of Complex Fluids* (Oxford University Press, New York, 1998).
[10]R. B. Bird, O. Hassager, R. C. Armstrong, and C. F. Curtiss, *Dynamics of Polymeric Liquids, Vol. 2, Kinetic Theory* (Wiley, New York, 1987).
[11]G. I. Taylor, "The formation of emulsions in definable fields of flow," Proc. R. Soc. London, Ser. A **146**, 501 (1934).
[12]G. G. Guller and L. G. Leal, "Flow birefringence of concentrated polymer solutions in two-dimensional flows," J. Polym. Sci., Polym. Phys. Ed. **19**, 557 (1981).
[13]B. J. Bentley and L. G. Leal, "A computer controlled four-roll mill for investigations of particle and rope dynamics in two-dimensional linear shear flows," J. Fluid Mech. **167**, 219 (1986).
[14]M. Renardy, "A comment on smoothness of viscoelastic stresses," J. Non-Newtonian Fluid Mech. **138**, 204 (2006).
[15]F. H. Lin, C. Liu, and P. Zhang, "On hydrodynamics of viscoelastic fluids," Commun. Pure Appl. Math. **58**, 1437 (2005).
[16]T. C. Sideris and B. Thomases, "Global existence for three-dimensional incompressible isotropic elastodynamics via the incompressible limit," Commun. Pure Appl. Math. **58**, 750 (2005).
[17]P. L. Lions and N. Masmoudi, "Global solutions for some Oldroyd models of non-Newtonian flows," Chin. Ann. Math., Ser. B **21**, 131 (2000).
[18]J. Y. Chemin and N. Masmoudi, "About lifespan of regular solutions of equations related to viscoelastic fluids," SIAM J. Math. Anal. **33**, 84 (2001).
[19]T. Y. Hou and R. Li, "Computing nearly singular solutions using pseudo-spectral methods," J. Comput. Phys. **226**, 379 (2007).
[20]R. Peyret, *Spectral Methods for Incompressible Viscous Flow* (Springer, New York, 2002).
[21]E. J. Hinch, "Mechanical models of dilute polymer solutions in strong flows," Phys. Fluids **20**, S22 (1977).
[22]C. Sulem, P. L. Sulem, and H. Frisch, "Tracing complex singularities with spectral methods," J. Comput. Phys. **50**, 138 (1981).
[23]R. Krasny, "A study of singularity formation in a vortex sheet by the point vortex approximation," J. Fluid Mech. **167**, 65 (1986).
[24]M. J. Shelley, "A study of singularity formation in vortex-sheet motion by a spectrally accurate vortex method," J. Fluid Mech. **244**, 493 (1992).
[25]R. B. Bird, P. J. Dotson, and N. L. Johnson, "Polymer solution rheology based on a finitely extensible bead-spring chain model," J. Non-Newtonian Fluid Mech. **7**, 213 (1980).
[26]R. G. Owens and T. N. Phillips, *Computational Rheology* (Imperial College Press, London, 2002).
[27]A. W. El-Kareh and L. G. Leal, "Existence of solutions for all Deborah numbers for a non-Newtonian model modified to include diffusion," J. Non-Newtonian Fluid Mech. **33**, 257 (1989).
[28]C.-Y. Lu, P. D. Olmsted, and R. C. Ball, "Effects of nonlocal stress on the determination of shear banding flow," Phys. Rev. Lett. **84**, 642 (2000).